Research Article

Iron Nanoparticles Encapsulated in S,N-Codoped Carbon: Sulfur Doping Enriches Surface Electron Density and Enhances Electrocatalytic Activity toward Oxygen Reduction

Shanyong Chen, Yong Yan, Panpan Hao, Muhong Li, Jiyuan Liang, Jia Guo, Yu Zhang, Shaowei Chen,* Weiping Ding, and Xuefeng Guo*

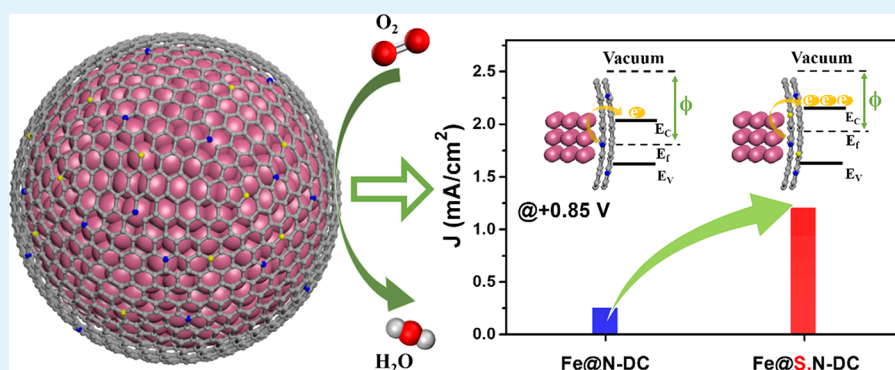Cite This: *ACS Appl. Mater. Interfaces* 2020, 12, 12686−12695

Read Online

ACCESS | Metrics & More | Article Recommendations | SI Supporting Information

ABSTRACT: Development of highly efficient nonprecious metal (NPM) catalysts for oxygen reduction reaction (ORR) in acidic media is challenging but of great significance. Herein, an effective ORR catalyst based on Fe nanoparticles encapsulated by S,N-codoped few-layer defective carbon (Fe@S,N-DC) was synthesized via a microwave-assisted strategy. The obtained Fe@S,N-DC nanocomposite showed a remarkable electrocatalytic activity toward ORR in acidic media, with a half-wave potential ($E_{1/2}$) of +0.785 V versus reversible hydrogen electrode, which was 80 mV more positive than that of the sulfur-free counterpart (Fe@N-DC). Furthermore, due to the protection by the S,N-codoped carbon shell, the Fe@S,N-DC nanocomposite displayed apparent stability with only a 13 mV negative shift of $E_{1/2}$ after 10,000 cycles and excellent tolerance to methanol. X-ray absorption near-edge spectroscopy measurements confirmed the formation of multiple defective sites on the S,N-codoped carbon surface and strong interfacial electron transfer from the Fe core to the outer carbon surface, as compared to the sulfur-free counterpart. The enriched electron density on the defective carbon surface of Fe@S,N-DC, induced by the interfacial electron transfer, facilitated the reduction of O_2 to OOH*, leading to enhanced ORR performance. These results shed light on the significance of S doping in Fe−N−C catalysts in the design of high-performance NPM catalysts for ORR in acidic media.

KEYWORDS: *nonprecious metal catalyst, metal@carbon composite, heteroatom doping, charge transfer, oxygen reduction reaction*

1. INTRODUCTION

Proton exchange membrane fuel cells (PEMFCs) have been identified as a promising energy conversion device due to minimal pollutant production and high-energy density.[1,2] There are two main reactions involved, oxygen reduction reaction (ORR) at the cathode and hydrogen oxidation reaction (HOR) at the anode. The sluggish electron-transfer kinetic of the ORR necessitates the use of a large amount of Pt-based catalysts, leading to high costs of PEMFCs, which impedes their widespread applications.[3] Therefore, development of highly efficient, nonprecious metal (NPM)-based ORR catalysts is of great significance for the large-scale application of PEMFCs.

Extensive studies have shown that iron−nitrogen−carbon (Fe−N−C) nanocomposites represent a promising alternative

to the Pt-based catalysts for ORR.[4−6] Unfortunately, due to the complex structures of the iron species (e.g., Fe_xO_y, Fe_3C, FeN_x, and Fe nanoparticles), it remains under active debates about the actual active sites for ORR. M−N_x moieties have been proposed as the ORR active sites since transition metals coordinated with the macrocyclic N_4 ligands were first reported as ORR catalysts in 1964.[7] Recently, Gewirth et al.[8]
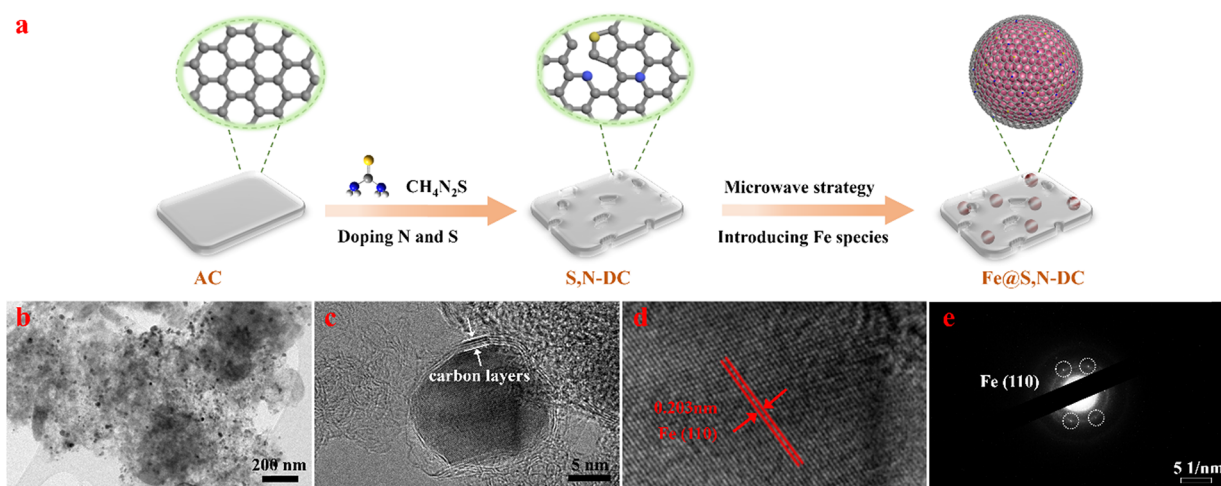
Figure 1. (a) Schematic illustration of the synthesis of Fe@S,N-DC. (b−d) TEM images at varied magnifications and (e) corresponding SAED patterns of Fe@S,N-DC.

have shown that the Fe−N$_x$ species within Fe−N−C could be selectively removed without compromising the ORR performance and argued that the Fe nanoparticles encapsulated within N-doped carbon layers were responsible for the ORR activity. Actually, in most studies the transition metal@carbon (TM@C) core@shell nanocomposites exhibit comparable or even better ORR activity than commercial Pt/C in alkaline media, but their activity in acidic media remains subpar as compared to that of Pt/C.[9−11] Notably, only the ORR process occurring in acidic media is in line with the actual operation condition of the PEMFCs.[12] Toward this end, Deng et al.[13] synthesized an ORR catalyst in which iron nanoparticles were encapsulated by pod-like carbon nanotubes (CNTs), and found that electron transfer from Fe nanoparticles to CNTs could lower the work function of the carbon surface, resulting in high ORR activity in acidic media. Interestingly, recent studies[14−16] have shown that codoping of N and S heteroatoms in the carbon framework can furtherly tailor the local electronic state and provide abundant defective carbon sites, leading to even better ORR performance. Inspired by these results, we anticipate that the incorporation of dual heteroatom dopants (such as N and S) into the outer carbon layer may enhance interfacial electron transfer in Fe@C nanocomposites and hence the ORR performance.

In fact, researchers have recently found that the ORR performance of the Fe−N−C catalysts can be further improved by the incorporation of S species.[17−26] Generally, S-doped Fe−N−C catalysts, possessing low loading and atomically dispersed Fe species, can be obtained by direct pyrolysis of Fe salts and N/S/C precursors and subsequent acid etching.[19,24,27,28] For example, Li et al.[27] embedded single Fe atoms into S- and N-codoped carbon by pyrolysis of pyrrole−thiophene copolymers and observed excellent ORR activity in alkaline media. Furthermore, pyrolysis of metal−organic frameworks[17,21] and template strategies[29,30] have been employed to prepare S-doped Fe−N−C with a porous structure and abundant exposed active sites. In corrosive acidic media, however, the exposed Fe sites can be easily etched during the ORR, leading to deterioration of the catalytic performance.[31,32] The core@shell structure of Fe@C nanocomposites is anticipated to exhibit strong tolerance to acid. Note that it is challenging to synthesize Fe@C in the presence of sulfur precursors because of the inevitable

generation of iron sulfides during the pyrolysis process.[21,22,25] Only a few studies have reported the preparation of S-doped Fe@C nanocomposites.[33,34] For example, Park et al.[34] recently reported the synthesis of an ORR catalyst with Fe nanoparticles encapsulated in a N,S-codoped graphitic shell (Fe@NSC) using a prereduction and two-step heating process, that is, prereduction of Fe salts and subsequent high-temperature treatment of Fe nanoparticles on N-doped carbon and N/S/C precursors. They then found that the introduction of sulfur species into the Fe@NC led to enhanced ORR activity and stability, with a negative shift of the half-wave potential ($E_{1/2}$) by only 41 mV after 10,000 potential cycles. However, the mechanistic origin of the enhanced ORR performance for S-doped Fe@C nanocomposites, in particular, within the context of the impact of S doping on interfacial electron transfer and catalytic activity, has remained largely unexplored.

Herein, we report a facile microwave-assisted strategy to prepare Fe@N,S-codoped carbon as highly efficient NPM catalysts for ORR in acidic media. The experimental procedure involves two major steps, (a) doping of S and N into the carbon matrix and (b) incorporation of Fe species into the S,N-doped defective carbon, leading to encapsulation of Fe nanoparticles within S,N-codoped few-layer defective carbon. The structures were characterized by a range of experimental techniques, such as X-ray photoelectron spectroscopy (XPS), X-ray absorption near-edge spectroscopy (XANES), and ultraviolet photoelectron spectroscopy (UPS). The results indicate enhanced electron transfer between the Fe nanoparticles and the S,N-codoped defective carbon (S,N-DC) layer, which led to enhanced ORR activity, as compared to the S-free counterpart. Meanwhile, the Fe@S,N-DC catalyst exhibited remarkable stability with only a −13 mV shift of the $E_{1/2}$ after 10,000 potential cycles and excellent tolerance to methanol due to the protection by the few-layer carbon against the corrosive acidic media.

2. RESULTS AND DISCUSSION

2.1. Structural Characterizations. As shown in Figure 1a, the preparation of Fe@S,N-DC involves two major steps (details in Section 4): (i) preparation of S,N-DC by pyrolysis of a mixture of activated carbon (AC) and thiourea and (ii) incorporation of iron species into the S,N-DC matrix by microwave radiation. It should be noted that the microwave-
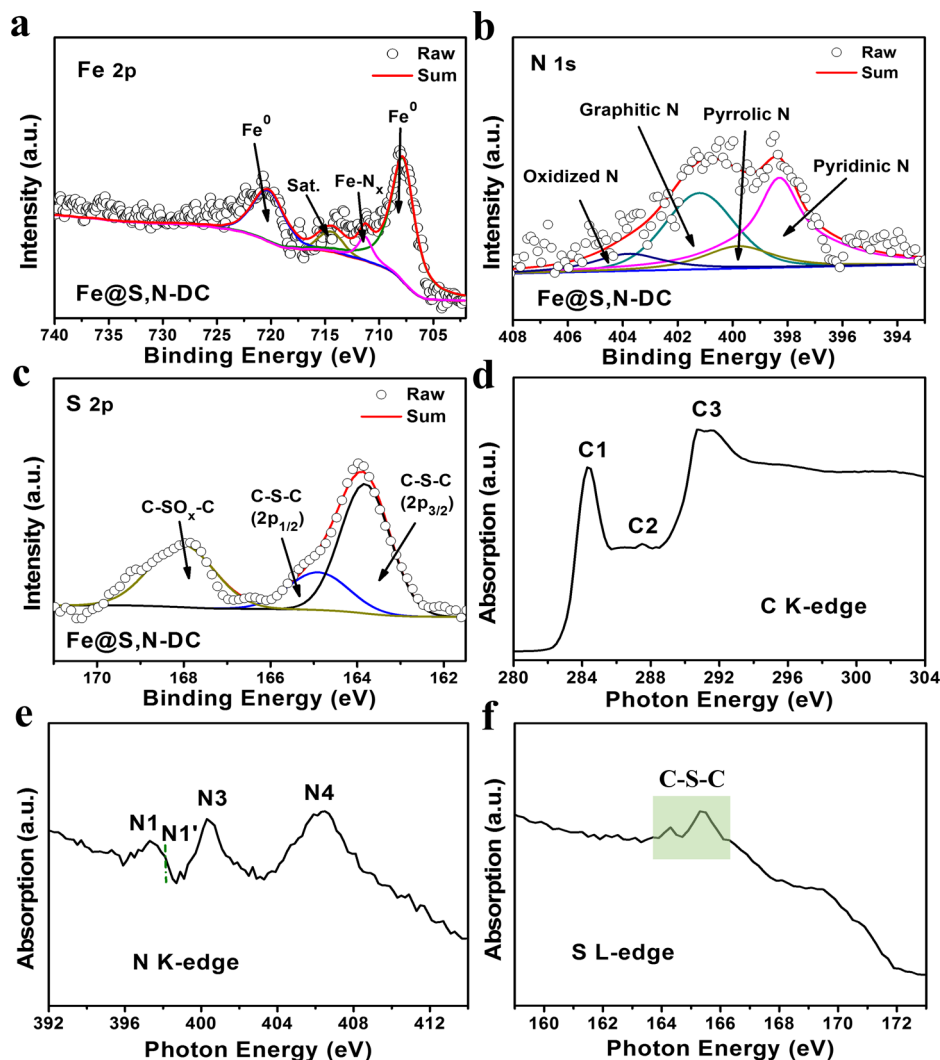
Figure 2. High-resolution XPS spectra of Fe@S,N-DC: (a) Fe 2p, (b) N 1s, and (c) S 2p. XANES spectra of Fe@S,N-DC: (d) C K-edge, (e) N K-edge, and (f) S L-edge.

assisted synthesis process is similar to chemical vapor deposition.[35,36] The iron salts were captured by the C−S−C species in S,N-DC and converted to melted iron nanoparticles under ultrafast microwave irradiation, and the S,N-DC substrate was partly dissolved into the melted iron nanoparticles. When the carbon concentration reached saturation, carbon began to spill out of the iron nanoparticles and transformed into a carbon shell. After acid etching and heat treatment under an inert atmosphere, the final samples consisted of Fe nanoparticles encapsulated within a S,N-codoped few-layer defective carbon shell. By contrast, for the Fe/S,N-DC sample that was prepared by traditional pyrolysis instead of the microwave-assisted route, the iron species were mostly atomically dispersed within the carbon matrix, forming Fe−N_x moieties rather than Fe@C structures.[19,20,27]

The structure of the obtained Fe@S,N-DC nanocomposites was first examined by TEM measurements (Figure 1b−d and Figure S1). From Figure 1b, the sample can be seen to consist of a number of dark-contrast nanoparticles of ca. 15 nm in diameter embedded within a low-contrast matrix. From the high-resolution TEM (HRTEM) images in Figure 1c,d, the nanoparticles can be seen to exhibit clearly defined lattice fringes with an interplanar spacing of 0.203 nm that is

consistent with the (110) crystalline planes of cubic iron (PDF #06-0696), and the nanoparticles were encapsulated within a few-layer graphitized carbon shell. Consistent results were obtained in selected area electron diffraction (SAED) measurements (Figure 1e). In addition, elemental mapping analysis based on energy-dispersive X-ray spectroscopy (EDS) (Figure S2) shows that N was homogeneously distributed within the carbon matrix, whereas S atoms were mostly localized around the Fe species, indicating that the iron nanoparticles interacted with the carbon shell mainly via the S and N dopants.

The elemental compositions and valence states of Fe@S,N-DC were then characterized by XPS measurements. From the Fe 2p spectrum in Figure 2a, one can see that the iron species mainly exist in the form of metallic iron,[37] with the $2p_{1/2}$ and $2p_{3/2}$ peaks at 707.8 and 720.1 eV, respectively, and a small fraction (ca. 1/10) of Fe−N_x (711.3 eV), consistent with HRTEM and XRD results. Figure 2b shows the N 1s spectrum, and deconvolution yields four N species in Fe@S,N-DC, pyridinic N (398.3 eV, 1.08 atom %), pyrrolic N (399.8 eV, 0.29 atom %), graphitic N (401.2 eV, 0.83 atom %), and oxidized N (403.8 eV, 0.24 atom %),[38,39] suggesting successful doping of nitrogen into the sample. The high concentrations of

pyridinic N and graphitic N are anticipated to be conducive for ORR electrocatalysis (vide infra).[40] The S 2p spectrum is shown in Figure 2c, which can be fitted with three subpeaks corresponding to C−S−C (S $2p_{3/2}$, 163.8 eV), C−S−C (S $2p_{1/2}$, 164.9 eV), and C−SO$_x$−C (168.0 eV) species.[29] The contents of C−S−C and C−SO$_x$−C species are estimated to be 0.154 and 0.066 atom %, suggesting that S was indeed doped into the carbon skeleton.

The XRD patterns of Fe@S,N-DC are displayed in Figure S3, where two major diffraction peaks can be seen. The broad peak centered at 2θ = 26° can be attributed to the diffraction of graphitic carbon, suggesting a good degree of graphitization of the sample by pyrolysis. A second peak can also be seen at 44.7°, consistent with the (110) diffraction of cubic iron (PDF #06-0696). For comparison, prior to acid etching, the corresponding sample also exhibited a series of diffraction peaks corresponding to Fe_3O_4 (PDF #19-0629), indicating effective removal of iron oxides by acid washing.

To gain further insights into the chemical configuration of the Fe@S,N-DC sample, XANES measurements were conducted. In the C K-edge spectrum in Figure 2d, there are two distinct peaks at 284.3 eV (C1) and 291.5 eV (C3), corresponding to the dipole transition of the 1s core electron of carbon to $\pi^*_{C=C}$ and σ^*_{C-C}, respectively,[41] while the C2 peak (287.5 eV) is related to the $\pi^*_{C-O/N/S-C}$ structure, which usually serves as the interfacial electron-transfer channel.[42] For the N K-edge XANES spectrum (Figure 2e), the N1 (397.4 eV; N1′, 398.1 eV) and N3 (400.4 eV) peaks are attributed to the C−N−C and N−3C,[43] that is, pyridinic N and graphitic N, respectively. Note that the split peaks of N1 and N1′ indicate that a fraction of pyridinic N interacted with Fe nanoparticles,[43] consistent with the XPS results. In other words, the interaction between the Fe nanoparticles and the S,N-codoped defective carbon (S,N-DC) shell was likely via the bridging Fe−N/S−C channel. The N4 peak likely arose from the σ^* transition of the C−N bond. As shown in Figure 2f, the splitting peaks in the region of 162 to 168 eV can be assigned to the C−S−C bonds.[43,44]

Notably, with microwave radiation prolonged to 3 and 5 min, the corresponding samples (denoted as Fe@S,N-DC$_3$ and Fe@S,N-DC$_5$) show a higher Fe loading (Figure S4a and Table S1) while having similar mesoporosity (Figure S4b) and Fe@C core@shell structures with larger nanoparticles and thicker outer carbon shells (Figure S5). In addition, nitrogen adsorption−desorption isotherm measurements showed that the specific surface area decreased with prolonged microwave radiation (Figure S4b and Table S1), consistent with the results of TEM analysis (Figure S5).

**2.2. Impacts of S and N Doping on ORR Performance.** As shown in Figure 3a,b, S,N-DC exhibited apparent enhancement of the ORR activity as compared to AC both in alkaline and acidic media. In 0.1 M KOH (Figure 3a), the ORR performance of S,N-DC exhibits a low $E_{1/2}$ of +0.818 V (only about 15 mV more negative than that of Pt/C, Table S3), low production of H_2O_2 (ca. 6%), and is close to the 4e⁻ reduction pathway (n = 3.88) within a wide range of electrode potential (Figure S6a). The limiting current was also significantly higher. This is likely due to the marked increase of the electrochemical surface area (ECSA) of S,N-DC, which is 16.6 times that of AC, as manifested in double-layer capacitance (Figure 3c), suggesting a drastically higher number of active sites created by S and N doping (for comparison, as displayed in Figure S7a, the BET surface areas of S,N-DC and
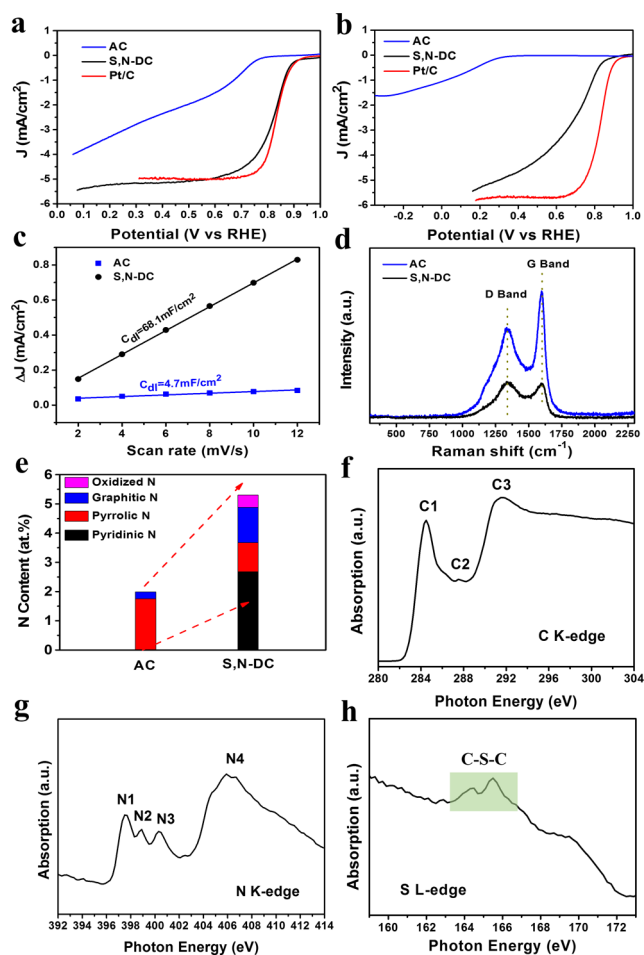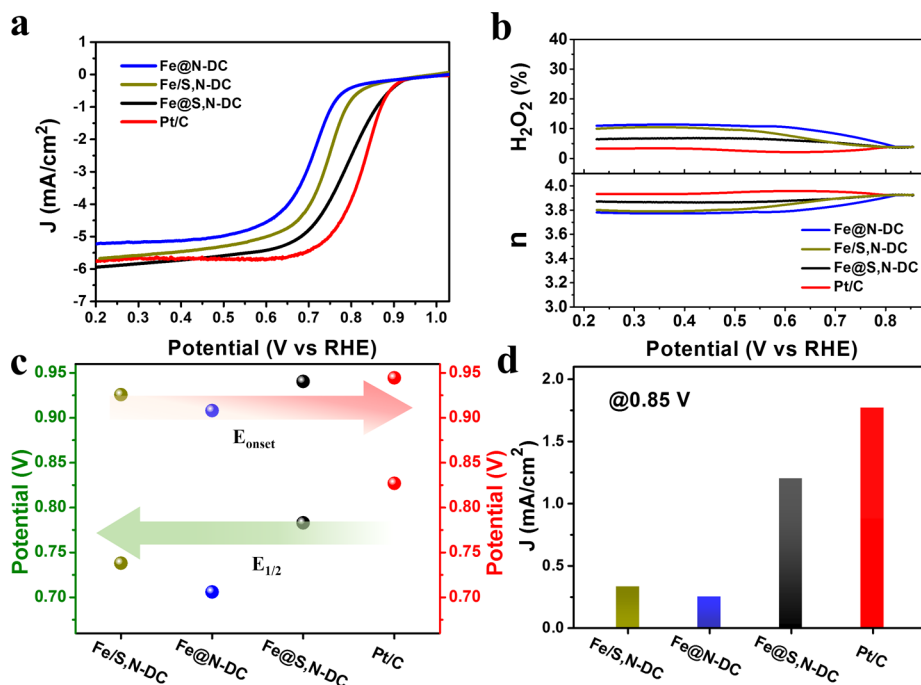

Figure 3. ORR polarization curves of AC, S,N-DC, and Pt/C in (a) 0.1 M KOH and (b) 0.1 M $HClO_4$. (c) Electrochemical active surface areas, (d) Raman spectra, and (e) N contents of S,N-DC and AC. (f) C K-edge, (g) N K-edge, and (h) S L-edge XANES spectra of S,N-DC.

AC were very comparable, at 1040 and 1381 m²/g, respectively). In addition, in Raman measurements (Figure 3d), the I_D/I_G ratio was found to increase from 0.71 for AC to 1.04 for S,N-DC, suggesting the formation of a more defective structure in S,N-DC. The formation of structural defects is also manifested in XPS (Figure S7b,d) and XANES (Figure 3f−h) measurements. From the XPS measurements, the contents of the N and S species of S,N-DC can be seen to increase to 5.25 and 1.35 atom % from 1.98 and 0 atom % for AC (Table S2), respectively. One can see that the XANES spectra of S,N-DC are similar to those of Fe@S,N-DC except for the integrated N1 peak and emerging N2 peak (pyrrolic N) in S,N-DC due to the absence of Fe species and the higher N content in S,N-DC.[14,43] Therefore, the increasing defect sites, in the forms of pyridinic N, graphitic N, and C−S−C species, are likely responsible for the enhanced ORR performance of S,N-DC. Furthermore, the smaller charge-transfer resistance (R_{ct}) of S,N-DC (Figure S7e) indicates faster electron transfer in the electrocatalytic process.

Nevertheless, in acidic media (Figure 3b), the ORR activity of the S,N-DC sample is markedly lower than that of Pt/C, with a more negative $E_{1/2}$ (by over 100 mV), lower n, and higher H_2O_2 yield (Figure S6b). Thus, further improvement is needed to achieve a better ORR performance, which can be
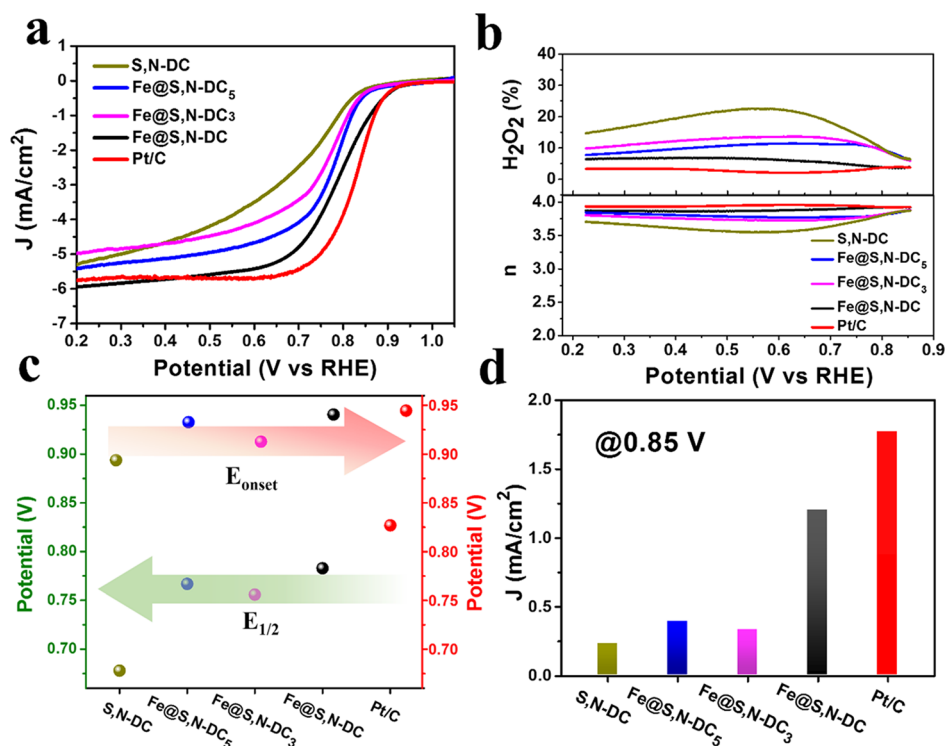
Figure 4. (a) ORR polarization curves of different catalysts in 0.1 M HClO$_4$. (b) Corresponding electron-transfer numbers (n) and hydrogen peroxide (H$_2$O$_2$) yields, (c) $E_{1/2}$ and E_{onset}, and (d) specific activity of the various catalysts at +0.85 V.


Figure 5. (a) ORR polarization curves of the series of samples in 0.1 M HClO$_4$. (b) Corresponding electron-transfer numbers (n) and hydrogen peroxide (H$_2$O$_2$) yields, (c) $E_{1/2}$ and E_{onset}, and (d) specific activity of the various samples at +0.85 V.

achieved by the incorporation of Fe nanoparticles, as detailed below.

2.3. Enhanced ORR Performance by the Incorporation of Iron Species. To further enhance the ORR activity of S,N-DC in acidic media, iron species are incorporated into the carbon matrix by a microwave-assisted strategy. From Figure 4 and Figure S8, it can be seen that in comparison to

S,N-DC, Fe@S,N-DC exhibits much enhanced ORR activity, which is also markedly better than those of Fe@S,N-DC$_3$ and Fe@S,N-DC$_5$, in terms of $E_{1/2}$, H$_2$O$_2$ yields, and kinetic current density. This may be attributed to the thick carbon shell in the latter (>5 layers) then impeded electron transfer from the metal core[45] and the formation of ORR active sites (Figure S9). Remarkably, the Fe@S,N-DC sample displays an
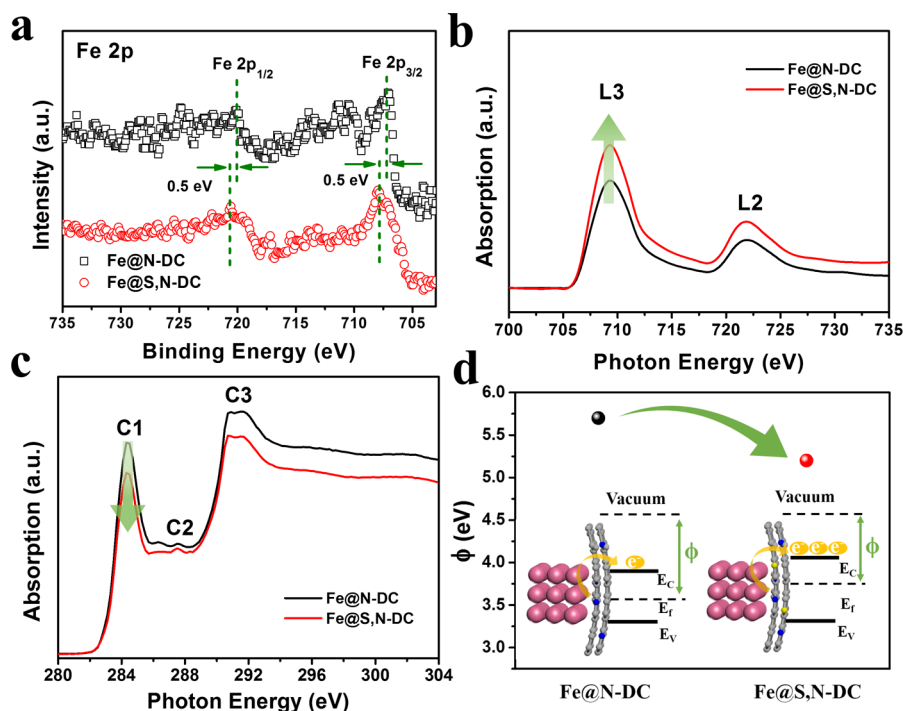
Figure 6. (a) Fe 2p XPS spectra, (b) Fe L-edge and (c) C K-edge XANES spectra, and (d) work function of Fe@N-DC and Fe@S,N-DC.

E_{onset} of +0.940 V that is comparable to that (+0.945 V) of Pt/C, only slightly lower $E_{1/2}$ (+0.785 V for Fe@S,N-DC and +0.827 V for Pt/C, note that the $E_{1/2}$ of Pt/C in the present study is highly comparable to those reported in the literature, Table S3), and similar specific activity (1.20 mA/cm^2 at +0.85 V for Fe@S,N-DC and 1.76 mA/cm^2 for Pt/C). This outstanding ORR performance makes Fe@S,N-DC one of the top NPM catalysts for the ORR in acidic media (Table S4). The low production of H_2O_2 (<6%) and high n values (>3.90) demonstrate that the 4e$^-$ reaction pathway dominated the ORR process by Fe@S,N-DC. Notably, in alkaline media, the ORR performance of Fe@S,N-DC is highly comparable to that of Pt/C (Figure S10).

It should be noted that Fe@S,N-DC displays a better ORR performance in acidic media than Fe/S,N-DC and the sulfur-free counterpart (Fe@N-DC). In fact, in comparison to Fe@N-DC, the Fe@S,N-DC sample exhibits a much more positive $E_{1/2}$ (by ca. 80 mV), lower yield of H_2O_2, and 4.88 times higher specific activity at +0.85 V (Figure 5 and Figure S11). Interestingly, according to results from ICP-AES, TEM, BET, TGA, and XPS measurements (Table S5 and Figures S12–S14), Fe@N-DC and Fe@S,N-DC show similar morphology, porous structure, Fe loading, and chemical states of the Fe and N elements. Therefore, the markedly enhanced ORR performance of Fe@S,N-DC suggests that the incorporation of sulfur plays a critical role in the improvement of the ORR activity.

As shown in Figure 6a, the Fe 2p binding energy ($2p_{1/2}$ and $2p_{3/2}$) can be found to blue-shift by 0.5 eV after the incorporation of sulfur, suggesting electron transfer from the Fe nanoparticles.[46,47] Meanwhile, the increasing intensity of the Fe L$_3$ peaks in Fe L-edge XANES spectra (Figure 6b) indicates increasing electron vacancies in the Fe 3d orbitals for Fe@S,N-DC,[48,49] consistent with the XPS results. From Figure 6c, one can see that the sp^2-hybridized $\pi^*_{C=C}$ structure (C1 peak) shows a decreasing intensity for Fe@S,N-DC, consistent with electron transfer from the Fe 3d orbitals to the C 2p

orbitals.[43,50,51] Such electron transfer became intensified upon the incorporation of sulfur. In addition, the more distinct C2 peak (Figure 6c) and the increasing I_D/I_G ratio (Figure S15) suggest the formation of more defective sites in the carbon shell of Fe@S,N-DC after the incorporation of sulfur.[52]

UPS measurements were then carried out to gain further insights into the interfacial electron transfer. As shown in Figure 6d and Figure S16, the work functions (ϕ) of Fe@S,N-DC and Fe@N-DC are estimated to be 5.2 and 5.7 eV, respectively, by using the ϕ of Au (5.1 eV) as the reference. The lower ϕ of Fe@S,N-DC is likely caused by the enriched electron density on the S,N-DC surface, indicating a smaller energy barrier for electron transfer from the material surface, which is favored for the reduction process.[49,53,54]

Meanwhile, as compared to Fe@N-DC, the Fe@S,N-DC sample shows a smaller semicircle in the Nyquist plot (Figure S17), indicating faster electron-transfer kinetics in the electrocatalytic reaction by S doping. The typical ORR pathway[55] is illustrated in Figure S18a, which includes four steps involving important intermediates like OOH*, O*, and OH*. For carbon-based materials, the formation of OOH* in the first step shows a relatively large Gibbs free energy and is usually identified as the rate-determining step.[56,57] This is because the low charge density or small density of states from the Fermi level on the sp^2 carbon surface impedes the adsorption of the oxygen molecule and the subsequent reduction to OOH*.[58,59] In the case of Fe@S,N-DC, the S,N-DC surface with enriched electrons can readily adsorb O_2 and facilitate the reduction to OOH* due to both the favorable electrostatic and covalent bonding at the interface.[13,60] Previous studies have shown that electron transfer occurs from the core metal to the N-doped carbon shell for M@N-C materials.[61–64] Herein, the incorporation of sulfur into the N-doped carbon shell boosts interfacial electron transfer in Fe@S,N-DC, which is most likely responsible for the enhanced ORR performance (Figure S18b).
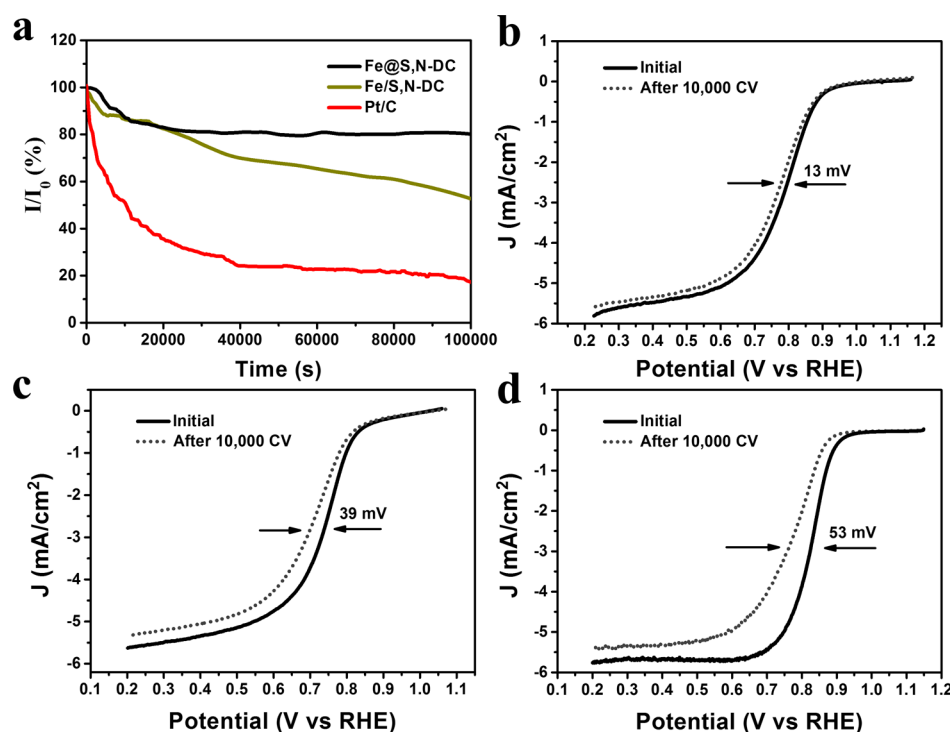
Figure 7. (a) Current–time (i–t) profiles of Fe@S,N-DC, Fe/S,N-DC, and Pt/C at +0.45 V for 100,000 s in 0.1 M HClO$_4$. (b–d) ORR polarization curves of (b) Fe@S,N-DC, (c) Fe/S,N-DC, and (d) Pt/C before and after 10,000 CV cycles in 0.1 M HClO$_4$.

2.4. Stability and Tolerance to Methanol. The stability of the obtained samples was then tested by chronoamperometric measurements at +0.45 V in an O$_2$-saturated 0.1 M HClO$_4$ solution (Figure 7a). Fe@S,N-DC retained about 80% of the initial current density after 100,000 s, which is significantly better than those of Pt/C (17%) and Fe/S,N-DC (53%). Moreover, after 10,000 CV cycles (Figure 7b–d), the $E_{1/2}$ of Fe@S,N-DC only shifted negatively by 13 mV, much smaller than those of Fe/S,N-DC (39 mV) and Pt/C (53 mV), which also surpassed leading results reported recently in the literature (Table S4). Interestingly, after 10,000 CV cycles, the morphology of Fe@S,N-DC remained virtually unchanged (Figure S19).

In direct methanol fuel cells, methanol is used as the fuel, which may cross over into the cathode compartment and poison the ORR catalyst. The methanol tolerance properties of Fe@S,N-DC and Pt/C were then examined and compared by CV and chronoamperometric measurements. From Figure S20a, one can see that upon the addition of methanol, Pt/C displayed a distinct voltammetric peak of methanol oxidation in replacement of the oxygen reduction peak, and the current density dropped to the 40% of the initial value (Figure S20b), demonstrating the distinct poisoning effect of Pt/C by methanol. In sharp contrast, addition of methanol did not result in an apparent variation of the voltammetric profiles of Fe@S,N-DC, confirming the strong tolerance to methanol. The excellent ORR activity, outstanding stability, and methanol tolerance suggest the great potential of Fe@S,N-DC as an ORR catalyst to replace Pt/C for dual exchange membrane fuel cell cathode, which is due to the formation of a quasi-Fe nanoparticle core@carbon shell nanostructure.

It should be noted that whereas Fe–N$_x$ moieties have been proposed to be responsible for the ORR activity of Fe,N-codoped carbon,[27] it is unlikely that such is the case in the present study. As shown in Figure S20c, the ORR polarization curves of Fe@S,N-DC remain virtually invariant before and after the addition of SCN$^-$, which is a well-known poisoning species for the metal centers, suggesting that Fe–N$_x$ moieties are unlikely the major ORR active sites in Fe@S,N-DC. For comparison, the control sample of Fe/S,N-DC exhibits apparent poisoning by SCN$^-$, with a negative shift of the $E_{1/2}$ by 26 mV (Figure S20d), suggesting apparent contributions of Fe–N$_x$ species to the ORR activity for Fe/S,N-DC. Oxygen temperature-programmed desorption (TPD) also has been conducted to investigate the possible contact between the encapsulated Fe and O$_2$. The TPD curves are similar for Fe@S,N-DC and S,N-DC (Figure S21), indicating indirect contact between Fe and O$_2$ in Fe@S,N-DC, that is, the outer S,N-DC shell serves as the reaction interface for the ORR.

3. CONCLUSIONS

In this study, a facile microwave-assisted strategy was developed for the synthesis of effective ORR catalysts where Fe nanoparticles were encapsulated by S,N-codoped few-layer defective carbon. The resulting nanocomposites were found to exhibit an impressive electrocatalytic activity toward ORR in both acidic and alkaline media, as compared to the S-free counterpart and Pt/C, which was ascribed to interfacial charge transfer from the encapsulated Fe nanoparticles to the carbon shell. Such a core–shell structure also led to remarkably enhanced stability (much better than Pt/C) and durability of the nanocomposites in acidic media. Importantly, the present facile strategy can be extended to other metal@carbon nanostructures for diverse electrocatalytic applications (Figures S22–S28).

4. EXPERIMENTAL SECTION

4.1. Sample Preparation. To prepare S,N-codoped defective carbon (S,N-DC), AC (1 g) was mixed with thiourea (5 g) via ball-

milling treatment for 10 min. Then, the collected mixture underwent a programmed heat treatment at 700 °C for 1 h and 800 °C for 2 h at a heating rate of 5 °C/min under Ar protection. N-doped defective carbon (N-DC) was prepared in the same way except that thiourea was replaced by urea.

To prepare Fe@S,N-DC, 0.513 g of S,N-DC, 1.27 g of $C_6H_{12}N_4$, and 0.513 g of Fe(OAc)$_2$OH were dispersed into 30 mL of H_2O to produce a homogeneous suspension under vigorous stirring for 12 h. The slurries were then collected by rotary evaporation at 40 °C and loaded into a 50 mL covered crucible. After microwave irradiation for 2 min (microwave oven power, 700 W), the obtained sample (denoted as Fe/S,N-DC$_{MW}$) was immersed into 0.5 M H_2SO_4 at 80 °C for 8 h to remove exposed Fe nanoparticles. After washing with water and ethanol several times and being dried at 80 °C, the powders were annealed at 700 °C for 1 h and then 800 °C for 2 h at a heating rate of 5 °C/min under an Ar flow. The sample was denoted as Fe@S,N-DC (with microwave treatment of 2 min).

Two additional samples were produced in the same manner except that the times of microwave treatment were 3 and 5 min and referred to as Fe@S,N-DC$_3$ and Fe@S,N-DC$_5$, respectively. The S-free counterpart, Fe@N-DC, was also prepared in the same procedure except that S,N-DC was replaced with N-DC.

■ ASSOCIATED CONTENT

ⓈⒾ Supporting Information

The Supporting Information is available free of charge at https://pubs.acs.org/doi/10.1021/acsami.9b20007.

Experimental section; characterization results; elemental content of AC and S,N-DC from XPS analysis; comparison of the ORR performance of the commercial Pt/C catalyst in this work and in the literature; comparison of the ORR performance of Fe@S,N-DC and relevant samples in the literature; Fe contents in Fe@S,N-DC, Fe/S,N-DC, and Fe@N-DC; TEM and HRTEM images; EDS elemental maps; XRD patterns; TGA curves; nitrogen adsorption−desorption isotherms; electron-transfer numbers (n) and hydrogen peroxide yields; XPS N 1s spectra; XPS S 2p spectrum; Nyquist plots; Tafel plots; kinetic current density; double-layer capacitance; ORR polarization curves; SAED patterns; Fe 2p and N 1s spectra; Raman spectra; UPS spectra; possible ORR pathway for Fe@S,N-DC; schematic illustrations of the electron transfer and ORR for Fe@S,N-DC; CV and current−time curves; oxygen TPD curves, and hydrogen evolution reaction performance (PDF)

■ AUTHOR INFORMATION

Corresponding Authors

Shaowei Chen — *Department of Chemistry and Biochemistry, University of California, Santa Cruz, California 95064, United States;* ⓄⒾ orcid.org/0000-0002-3668-8551; Email: shaowei@ucsc.edu

Xuefeng Guo — *Key Laboratory of Mesoscopic Chemistry, Ministry of Education, School of Chemistry and Chemical Engineering, Nanjing University, Nanjing 210023, China;* ⓄⒾ orcid.org/0000-0002-5492-5899; Email: guoxf@nju.edu.cn

Authors

Shanyong Chen — *Key Laboratory of Mesoscopic Chemistry, Ministry of Education, School of Chemistry and Chemical Engineering, Nanjing University, Nanjing 210023, China*

Yong Yan — *Key Laboratory of Mesoscopic Chemistry, Ministry of Education, School of Chemistry and Chemical Engineering, Nanjing University, Nanjing 210023, China*

Panpan Hao — *Key Laboratory of Mesoscopic Chemistry, Ministry of Education, School of Chemistry and Chemical Engineering, Nanjing University, Nanjing 210023, China*

Muhong Li — *Key Laboratory of Mesoscopic Chemistry, Ministry of Education, School of Chemistry and Chemical Engineering, Nanjing University, Nanjing 210023, China*

Jiyuan Liang — *Key Laboratory of Optoelectronic Chemical Materials and Devices, Ministry of Education, School of Chemical and Environmental Engineering, Jianghan University, Wuhan 430056, China*

Jia Guo — *Key Laboratory of Mesoscopic Chemistry, Ministry of Education, School of Chemistry and Chemical Engineering, Nanjing University, Nanjing 210023, China*

Yu Zhang — *Key Laboratory of Mesoscopic Chemistry, Ministry of Education, School of Chemistry and Chemical Engineering, Nanjing University, Nanjing 210023, China*

Weiping Ding — *Key Laboratory of Mesoscopic Chemistry, Ministry of Education, School of Chemistry and Chemical Engineering, Nanjing University, Nanjing 210023, China;* ⓄⒾ orcid.org/0000-0002-8034-5740

Complete contact information is available at:
https://pubs.acs.org/10.1021/acsami.9b20007

Notes

The authors declare no competing financial interest.

■ ACKNOWLEDGMENTS

■ REFERENCES

(1) Chong, L.; Wen, J.; Kubal, J.; Sen, F. G.; Zou, J.; Greeley, J.; Chan, M.; Barkholtz, H.; Ding, W.; Liu, D.-J. Ultralow-Loading Platinum-Cobalt Fuel Cell Catalysts Derived from Imidazolate Frameworks. *Science* **2018**, *362*, 1276−1281.

(2) Tang, H.; Zeng, Y.; Liu, D.; Qu, D.; Luo, J.; Binnemans, K.; De Vos, D. E.; Fransaer, J.; Qu, D.; Sun, S.-G. Dual-Doped Mesoporous Carbon Synthesized by a Novel Nanocasting Method with Superior Catalytic Activity for Oxygen Reduction. *Nano Energy* **2016**, *26*, 131−138.

(3) Chen, T.; Xu, Y.; Guo, S.; Wei, D.; Peng, L.; Guo, X.; Xue, N.; Zhu, Y.; Chen, Z.; Zhao, B.; Ding, W. Ternary Heterostructural Pt/CN$_x$/Ni as a Supercatalyst for Oxygen Reduction. *Iscience* **2019**, *11*, 388−397.

(4) Malko, D.; Kucernak, A.; Lopes, T. In Situ Electrochemical Quantification of Active Sites in Fe−N/C Non-Precious Metal Catalysts. *Nat. Commun.* **2016**, *7*, 13285.

(5) Zhong, L.; Frandsen, C.; Mørup, S.; Hu, Y.; Pan, C.; Cleemann, L. N.; Jensen, J. O.; Li, Q. ^{57}Fe-Mössbauer Spectroscopy and Electrochemical Activities of Graphitic Layer Encapsulated Iron

Electrocatalysts for the Oxygen Reduction Reaction. *Appl. Catal., B* **2018**, *221*, 406−412.

(6) Peng, Y.; Chen, S. Electrocatalysts Based on Metal@Carbon Core@Shell Nanocomposites: An Overview. *Green Energy Environ.* **2018**, *3*, 335−351.

(7) Jasinski, R. A New Fuel Cell Cathode Catalyst. *Nature* **1964**, *201*, 1212−1213.

(8) Varnell, J. A.; Tse, E. C. M.; Schulz, C. E.; Fister, T. T.; Haasch, R. T.; Timoshenko, J.; Frenkel, A. I.; Gewirth, A. A. Identification of Carbon-Encapsulated Iron Nanoparticles as Active Species in Non-Precious Metal Oxygen Reduction Catalysts. *Nat. Commun.* **2016**, *7*, 12582.

(9) Jiang, H.; Liu, Y.; Hao, J.; Wang, Y.; Li, W.; Li, J. Self-Assembly Synthesis of Cobalt- and Nitrogen-Coembedded Trumpet Flower-Like Porous Carbons for Catalytic Oxygen Reduction in Alkaline and Acidic Media. *ACS Sustainable Chem. Eng.* **2017**, *5*, 5341−5350.

(10) Jiang, H.; Yao, Y.; Zhu, Y.; Liu, Y.; Su, Y.; Yang, X.; Li, C. Iron Carbide Nanoparticles Encapsulated in Mesoporous Fe-N-Doped Graphene-Like Carbon Hybrids as Efficient Bifunctional Oxygen Electrocatalysts. *ACS Appl. Mater. Interfaces* **2015**, *7*, 21511−21520.

(11) Xiao, M.; Zhu, J.; Feng, L.; Liu, C.; Xing, W. Meso/Macroporous Nitrogen-Doped Carbon Architectures with Iron Carbide Encapsulated in Graphitic Layers as an Efficient and Robust Catalyst for the Oxygen Reduction Reaction in Both Acidic and Alkaline Solutions. *Adv. Mater.* **2015**, *27*, 2521−2527.

(12) Mun, Y.; Lee, S.; Kim, K.; Kim, S.; Lee, S.; Han, J. W.; Lee, J. Versatile Strategy for Tuning ORR Activity of a Single Fe-N_4 Site by Controlling Electron-Withdrawing/Donating Properties of a Carbon Plane. *J. Am. Chem. Soc.* **2019**, *141*, 6254−6262.

(13) Deng, D.; Yu, L.; Chen, X.; Wang, G.; Jin, L.; Pan, X.; Deng, J.; Sun, G.; Bao, X. Iron Encapsulated within Pod-like Carbon Nanotubes for Oxygen Reduction Reaction. *Angew. Chem., Int. Ed.* **2013**, *52*, 371−375.

(14) Li, D.; Jia, Y.; Chang, G.; Chen, J.; Liu, H.; Wang, J.; Hu, Y.; Xia, Y.; Yang, D.; Yao, X. A Defect-Driven Metal-free Electrocatalyst for Oxygen Reduction in Acidic Electrolyte. *Chem* **2018**, *4*, 2345−2356.

(15) Yang, J.; Xiang, F.; Guo, H.; Wang, L.; Niu, X. Honeycomb-Like Porous Carbon with N and S Dual-Doping as Metal-Free Catalyst for the Oxygen Reduction Reaction. *Carbon* **2020**, *156*, 514−522.

(16) Villemson, K. M.; Kaare, K.; Raudsepp, R.; Käämbre, T.; Šmits, K.; Wang, P.; Kuzmin, A. V.; Sutka, A.; Shainyan, B. A.; Kruusenberg, I. Identification of Active Sites for Oxygen Reduction Reaction on Nitrogen- and Sulfur-Codoped Carbon Catalysts. *J. Phys. Chem. C* **2019**, *123*, 16065−16074.

(17) Jin, H.; Zhou, H.; Li, W.; Wang, Z.; Yang, J.; Xiong, Y.; He, D.; Chen, L.; Mu, S. In Situ Derived Fe/N/S-Codoped Carbon Nanotubes from ZIF-8 Crystals as Efficient Electrocatalysts for the Oxygen Reduction Reaction and Zinc-Air Batteries. *J. Mater. Chem. A* **2018**, *6*, 20093−20099.

(18) Zhu, Y.; Chen, X.; Liu, J.; Zhang, J.; Xu, D.; Peng, W.; Li, Y.; Zhang, G.; Zhang, F.; Fan, X. Rational Design of Fe/N/S-Doped Nanoporous Carbon Catalysts from Covalent Triazine Frameworks for Efficient Oxygen Reduction. *ChemSusChem* **2018**, *11*, 2402−2409.

(19) Zhang, J.; Zhang, M.; Zeng, Y.; Chen, J.; Qiu, L.; Zhou, H.; Sun, C.; Yu, Y.; Zhu, C.; Zhu, Z. Single Fe Atom on Hierarchically Porous S, N-Codoped Nanocarbon Derived from Porphyra Enable Boosted Oxygen Catalysis for Rechargeable Zn-Air Batteries. *Small* **2019**, *15*, 1900307.

(20) Shu, C.; Chen, Y.; Yang, X.-D.; Liu, Y.; Chong, S.; Fang, Y.; Liu, Y.; Yang, W.-H. Enhanced Fe Dispersion via "Pinning" Effect of Thiocyanate Ion on Ferric Ion in Fe-N-S-Doped Catalyst as an Excellent Oxygen Reduction Reaction Electrode. *J. Power Sources* **2018**, *376*, 161−167.

(21) Zhang, C.; An, B.; Yang, L.; Wu, B.; Shi, W.; Wang, Y.-C.; Long, L.-S.; Wang, C.; Lin, W. Sulfur-Doping Achieves Efficient Oxygen Reduction in Pyrolyzed Zeolitic Imidazolate Frameworks. *J. Mater. Chem. A* **2016**, *4*, 4457−4463.

(22) Xiao, J.; Xia, Y.; Hu, C.; Xi, J.; Wang, S. Raisin Bread-Like Iron Sulfides/Nitrogen and Sulfur Dual-Doped Mesoporous Graphitic Carbon Spheres: a Promising Electrocatalyst for the Oxygen Reduction Reaction in Alkaline and Acidic Media. *J. Mater. Chem. A* **2017**, *5*, 11114−11123.

(23) Qiao, Y.; Yuan, P.; Hu, Y.; Zhang, J.; Mu, S.; Zhou, J.; Li, H.; Xia, H.; He, J.; Xu, Q. Sulfuration of an Fe-N-C Catalyst Containing Fe_xC/Fe Species to Enhance the Catalysis of Oxygen Reduction in Acidic Media and for Use in Flexible Zn-Air Batteries. *Adv. Mater.* **2018**, *30*, 1804504.

(24) Wang, Y.-C.; Lai, Y.-J.; Song, L.; Zhou, Z.-Y.; Liu, J.-G.; Wang, Q.; Yang, X.-D.; Chen, C.; Shi, W.; Zheng, Y.-P.; Rauf, M.; Sun, S.-G. S-Doping of an Fe/N/C ORR Catalyst for Polymer Electrolyte Membrane Fuel Cells with High Power Density. *Angew. Chem., Int. Ed.* **2015**, *54*, 9907−9910.

(25) Kramm, U. I.; Herrmann-Geppert, I.; Fiechter, S.; Zehl, G.; Zizak, I.; Dorbandt, I.; Schmeißer, D.; Bogdanoff, P. Effect of Iron-Carbide Formation on the Number of Active Sites in Fe-N-C Catalysts for the Oxygen Reduction Reaction in Acidic Media. *J. Mater. Chem. A* **2014**, *2*, 2663−2670.

(26) Kiciński, W.; Dembinska, B.; Norek, M.; Budner, B.; Polański, M.; Kulesza, P. J.; Dyjak, S. Heterogeneous Iron-Containing Carbon Gels as Catalysts for Oxygen Electroreduction: Multifunctional Role of Sulfur in the Formation of Efficient Systems. *Carbon* **2017**, *116*, 655−669.

(27) Li, Q.; Chen, W.; Xiao, H.; Gong, Y.; Li, Z.; Zheng, L.; Zheng, X.; Yan, W.; Cheong, W.-C.; Shen, R.; Fu, N.; Gu, L.; Zhuang, Z.; Chen, C.; Wang, D.; Peng, Q.; Li, J.; Li, Y. Fe Isolated Single Atoms on S, N Codoped Carbon by Copolymer Pyrolysis Strategy for Highly Efficient Oxygen Reduction Reaction. *Adv. Mater.* **2018**, *30*, 1800588.

(28) Wu, M.; Tang, Q.; Dong, F.; Bai, Z.; Zhang, L.; Qiao, J. Fe/N/S-Composited Hierarchically Porous Carbons with Optimized Surface Functionality, Composition and Nanoarchitecture as Electrocatalysts for Oxygen Reduction Reaction. *J. Catal.* **2017**, *352*, 208−217.

(29) Shen, H.; Gracia-Espino, E.; Ma, J.; Zang, K.; Luo, J.; Wang, L.; Gao, S.; Mamat, X.; Hu, G.; Wagberg, T.; Guo, S. Synergistic Effects between Atomically Dispersed Fe-N-C and C-S-C for the Oxygen Reduction Reaction in Acidic Media. *Angew. Chem., Int. Ed.* **2017**, *56*, 13800−13804.

(30) Kwak, D.-H.; Han, S.-B.; Kim, D.-H.; Won, J.-E.; Park, K.-W. Amino Acid-Derived Non-Precious Catalysts with Excellent Electro-catalytic Performance and Methanol Tolerance in Oxygen Reduction Reaction. *Appl. Catal., B* **2018**, *238*, 93−103.

(31) Banham, D.; Ye, S.; Pei, K.; Ozaki, J.-I.; Kishimoto, T.; Imashiro, Y. A Review of the Stability and Durability of Non-Precious Metal Catalysts for the Oxygen Reduction Reaction in Proton Exchange Membrane Fuel Cells. *J. Power Sources* **2015**, *285*, 334−348.

(32) Baranton, S.; Coutanceau, C.; Roux, C.; Hahn, F.; Léger, J.-M. Oxygen Reduction Reaction in Acid Medium at Iron Phthalocyanine Dispersed on High Surface Area Carbon Substrate: Tolerance to Methanol, Stability and Kinetics. *J. Electroanal. Chem.* **2005**, *577*, 223−234.

(33) Eissa, A. A.; Peera, S. G.; Kim, N. H.; Lee, J. H. g-C_3N_4 Templated Synthesis of the Fe_3C@NSC Electrocatalyst Enriched with Fe-N_x Active Sites for Efficient Oxygen Reduction Reaction. *J. Mater. Chem. A* **2019**, *7*, 16920−16936.

(34) Park, H.-S.; Han, S.-B.; Kwak, D.-H.; Han, J.-H.; Park, K.-W. Fe Nanoparticles Encapsulated in Doped Graphitic Shells as High-Performance and Stable Catalysts for Oxygen Reduction Reaction in an Acid Medium. *J. Catal.* **2019**, *370*, 130−137.

(35) Pentsak, E. O.; Gordeev, E. G.; Ananikov, V. P. Noninnocent Nature of Carbon Support in Metal/Carbon Catalysts: Etching/Pitting vs Nanotube Growth under Microwave Irradiation. *ACS Catal.* **2014**, *4*, 3806−3814.

(36) Bu, F.; Chen, W.; Gu, J.; Agboola, P. O.; Al-Khalli, N. F.; Shakir, I.; Xu, Y. Microwave-Assisted CVD-Like Synthesis of Dispersed Monolayer/Few-Layer N-Doped Graphene Encapsulated Metal Nanocrystals for Efficient Electrocatalytic Oxygen Evolution. *Chem. Sci.* **2018**, *9*, 7009−7016.

(37) Meng, F.-L.; Wang, Z.-L.; Zhong, H.-X.; Wang, J.; Yan, J.-M.; Zhang, X.-B. Reactive Multifunctional Template-Induced Preparation of Fe-N-Doped Mesoporous Carbon Microspheres Towards Highly Efficient Electrocatalysts for Oxygen Reduction. *Adv. Mater.* **2016**, *28*, 7948−7955.

(38) Fan, W.; Li, Z.; You, C.; Zong, X.; Tian, X.; Miao, S.; Shu, T.; Li, C.; Liao, S. Binary Fe, Cu-Doped Bamboo-Like Carbon Nanotubes as Efficient Catalyst for the Oxygen Reduction Reaction. *Nano Energy* **2017**, *37*, 187−194.

(39) Chen, S.; Bi, F.; Xiang, K.; Zhang, Y.; Hao, P.; Li, M.; Zhao, B.; Guo, X. Reactive Template-Derived CoFe/N-Doped Carbon Nanosheets as Highly Efficient Electrocatalysts toward Oxygen Reduction, Oxygen Evolution, and Hydrogen Evolution. *ACS Sustainable Chem. Eng.* **2019**, *7*, 15278−15288.

(40) Lai, L.; Potts, J. R.; Zhan, D.; Wang, L.; Poh, C. K.; Tang, C.; Gong, H.; Shen, Z.; Lin, J.; Ruoff, R. S. Exploration of the Active Center Structure of Nitrogen-Doped Graphene-Based Catalysts for Oxygen Reduction Reaction. *Energy Environ. Sci.* **2012**, *5*, 7936−7942.

(41) Zheng, Y.; Jiao, Y.; Zhu, Y.; Li, L. H.; Han, Y.; Chen, Y.; Du, A.; Jaroniec, M.; Qiao, S. Z. Hydrogen Evolution by a Metal-Free Electrocatalyst. *Nat. Commun.* **2014**, *5*, 3783.

(42) Chen, P.; Zhang, N.; Wang, S.; Zhou, T.; Tong, Y.; Ao, C.; Yan, W.; Zhang, L.; Chu, W.; Wu, C.; Xie, Y. Interfacial Engineering of Cobalt Sulfide/Graphene Hybrids for Highly Efficient Ammonia Electrosynthesis. *Proc. Natl. Acad. Sci. U. S. A.* **2019**, *116*, 6635−6640.

(43) Chen, P.; Zhou, T.; Xing, L.; Xu, K.; Tong, Y.; Xie, H.; Zhang, L.; Yan, W.; Chu, W.; Wu, C.; Xie, Y. Atomically Dispersed Iron-Nitrogen Species as Electrocatalysts for Bifunctional Oxygen Evolution and Reduction Reactions. *Angew. Chem., Int. Ed.* **2017**, *56*, 610−614.

(44) Sarret, G.; Connan, J.; Kasrai, M.; Bancroft, G. M.; Charrié-Duhaut, A.; Lemoine, S.; Adam, P.; Albrecht, P.; Eybert-Bérard, L. Chemical Forms of Sulfur in Geological and Archeological Asphaltenes from Middle East, France, and Spain Determined by Sulfur K- and L-Edge X-Ray Absorption Near-Edge Structure Spectroscopy. *Geochim. Cosmochim. Acta* **1999**, *63*, 3767−3779.

(45) Deng, J.; Yu, L.; Deng, D.; Chen, X.; Yang, F.; Bao, X. Highly Active Reduction of Oxygen on a FeCo Alloy Catalyst Encapsulated in Pod-like Carbon Nanotubes with Fewer Walls. *J. Mater. Chem. A* **2013**, *1*, 14868−14873.

(46) Fu, T.; Wang, M.; Cai, W.; Cui, Y.; Gao, F.; Peng, L.; Chen, W.; Ding, W. Acid-Resistant Catalysis without Use of Noble Metals: Carbon Nitride with Underlying Nickel. *ACS Catal.* **2014**, *4*, 2536−2543.

(47) Xue, Z.-H.; Han, J.-T.; Feng, W.-J.; Yu, Q.-Y.; Li, X.-H.; Antonietti, M.; Chen, J.-S. Tuning the Adsorption Energy of Methanol Molecules Along Ni-N-Doped Carbon Phase Boundaries by the Mott-Schottky Effect for Gas-Phase Methanol Dehydrogenation. *Angew. Chem., Int. Ed.* **2018**, *57*, 2697−2701.

(48) Zhong, J.; Zhang, H.; Sun, X.; Lee, S.-T. Synchrotron Soft X-ray Absorption Spectroscopy Study of Carbon and Silicon Nanostructures for Energy Applications. *Adv. Mater.* **2014**, *26*, 7786−7806.

(49) Lin, Y.; Yang, L.; Zhang, Y.; Jiang, H.; Xiao, Z.; Wu, C.; Zhang, G.; Jiang, J.; Song, L. Defective Carbon-CoP Nanoparticles Hybrids with Interfacial Charges Polarization for Efficient Bifunctional Oxygen Electrocatalysis. *Adv. Energy Mater.* **2018**, *8*, 1703623.

(50) Lee, V.; Whittaker, L.; Jaye, C.; Baroudi, K. M.; Fischer, D. A.; Banerjee, S. Large-Area Chemically Modified Graphene Films: Electrophoretic Deposition and Characterization by Soft X-ray Absorption Spectroscopy. *Chem. Mater.* **2009**, *21*, 3905−3916.

(51) Pacilé, D.; Papagno, M.; Rodríguez, A. F.; Grioni, M.; Papagno, L.; Girit, Ç. Ö.; Meyer, J. C.; Begtrup, G. E.; Zettl, A. Near-Edge X-Ray Absorption Fine-Structure Investigation of Graphene. *Phys. Rev. Lett.* **2008**, *101*, No. 066806.

(52) Jia, Y.; Zhang, L.; Zhuang, L.; Liu, H.; Yan, X.; Wang, X.; Liu, J.; Wang, J.; Zheng, Y.; Xiao, Z.; Taran, E.; Chen, J.; Yang, D.; Zhu, Z.; Wang, S.; Dai, L.; Yao, X. Identification of Active Sites for Acidic Oxygen Reduction on Carbon Catalysts with and without Nitrogen Doping. *Nat. Catal.* **2019**, 688.

(53) Lee, D. H.; Lee, W. J.; Lee, W. J.; Kim, S. O.; Kim, Y.-H. Theory, Synthesis, and Oxygen Reduction Catalysis of Fe-Porphyrin-Like Carbon Nanotube. *Phys. Rev. Lett.* **2011**, *106*, 175502.

(54) Li, X.; Liu, W.; Zhang, M.; Zhong, Y.; Weng, Z.; Mi, Y.; Zhou, Y.; Li, M.; Cha, J. J.; Tang, Z.; Jiang, H.; Li, X.; Wang, H. Strong Metal-Phosphide Interactions in Core-Shell Geometry for Enhanced Electrocatalysis. *Nano Lett.* **2017**, *17*, 2057−2063.

(55) Shen, X.; Nagai, T.; Yang, F.; Zhou, L. Q.; Pan, Y.; Yao, L.; Wu, D.; Liu, Y.-S.; Feng, J.; Guo, J.; Jia, H.; Peng, Z. Dual-Site Cascade Oxygen Reduction Mechanism on SnO$_x$/Pt-Cu-Ni for Promoting Reaction Kinetics. *J. Am. Chem. Soc.* **2019**, *141*, 9463−9467.

(56) Li, M.; Zhang, L.; Xu, Q.; Niu, J.; Xia, Z. N-doped Graphene as Catalysts for Oxygen Reduction and Oxygen Evolution Reactions: Theoretical Considerations. *J. Catal.* **2014**, *314*, 66−72.

(57) Chai, G.-L.; Hou, Z.; Shu, D.-J.; Ikeda, T.; Terakura, K. Active Sites and Mechanisms for Oxygen Reduction Reaction on Nitrogen-Doped Carbon Alloy Catalysts: Stone-Wales Defect and Curvature Effect. *J. Am. Chem. Soc.* **2014**, *136*, 13629−13640.

(58) Lu, B.; Smart, T. J.; Qin, D.; Lu, J. E.; Wang, N.; Chen, L.; Peng, Y.; Ping, Y.; Chen, S. Nitrogen and Iron-Codoped Carbon Hollow Nanotubes as High-Performance Catalysts toward Oxygen Reduction Reaction: A Combined Experimental and Theoretical Study. *Chem. Mater.* **2017**, *29*, 5617−5628.

(59) Wang, N.; Lu, B.; Li, L.; Niu, W.; Tang, Z.; Kang, X.; Chen, S. Graphitic Nitrogen Is Responsible for Oxygen Electroreduction on Nitrogen-Doped Carbons in Alkaline Electrolytes: Insights from Activity Attenuation Studies and Theoretical Calculations. *ACS Catal.* **2018**, *8*, 6827−6836.

(60) Zhang, L.; Xia, Z. Mechanisms of Oxygen Reduction Reaction on Nitrogen-Doped Graphene for Fuel Cells. *J. Phys. Chem. C* **2011**, *115*, 11170−11176.

(61) Tu, Y.; Ren, P.; Deng, D.; Bao, X. Structural and Electronic Optimization of Graphene Encapsulating Binary Metal for Highly Efficient Water Oxidation. *Nano Energy* **2018**, *52*, 494−500.

(62) Yang, Y.; Lin, Z.; Gao, S.; Su, J.; Lun, Z.; Xia, G.; Chen, J.; Zhang, R.; Chen, Q. Tuning Electronic Structures of Nonprecious Ternary Alloys Encapsulated in Graphene Layers for Optimizing Overall Water Splitting Activity. *ACS Catal.* **2017**, *7*, 469−479.

(63) Deng, J.; Ren, P.; Deng, D.; Bao, X. Enhanced Electron Penetration through an Ultrathin Graphene Layer for Highly Efficient Catalysis of the Hydrogen Evolution Reaction. *Angew. Chem., Int. Ed.* **2015**, *54*, 2100−2104.

(64) Cui, X.; Ren, P.; Deng, D.; Deng, J.; Bao, X. Single Layer Graphene Encapsulating Non-Precious Metals as High-Performance Electrocatalysts for Water Oxidation. *Energy Environ. Sci.* **2016**, *9*, 123−129.